

## Coherency calculations in the presence of structural dip

Kurt J. Marfurt\*, V. Sudhaker<sup>‡</sup>, Adam Gersztenkorn\*,  
Kelly D. Crawford\*\*, and Susan E. Nissen\*

### ABSTRACT

We have used crosscorrelation, semblance, and eigenstructure algorithms to estimate coherency. The first two algorithms calculate coherency over a multiplicity of trial time lags or dips, with the dip having the highest coherency corresponding to the local dip of the reflector. Partially because of its greater computational cost, our original eigenstructure algorithm calculated coherency along an implicitly flat horizon. Although generalizing the eigenstructure algorithm to search over a range of test dips allowed us to image coherency in the presence of steeply dipping structures, we were somewhat surprised that this generalization concomitantly degenerated the quality of the fault images in flatter dip areas.

Because it is a local estimation of reflector dip (including as few as five traces), the multidip coherency estimate provides an algorithmically correct, but interpretationally undesirable, estimate of the best apparent dip that explained the offset reflectors across a fault. We ameliorate this problem using two methods, both of which require the smoothing of a locally inaccurate estimate of regional dip. We then calculate our eigenstructure estimate of coherency only along the dip of the reflector, thereby providing maximum lateral resolution of reflector discontinuities. We are thus both better able to explain the superior results obtained by our earliest eigenstructure analysis along interpreted horizon slices, yet able to extend this resolution to steeply dipping reflectors on uninterpreted cubes of seismic data.

### INTRODUCTION

The original, crosscorrelation based (or  $c_1$ ) coherency algorithm developed by Bahorich and Farmer (1995) provided interpreters with a new way of visualizing faults and stratigraphic features in 3-D seismic data volumes. By providing the structural framework before actual interpretation began, the “coherency cube” has greatly reduced the cycle time needed to perform a conventional 3-D interpretation. Through more careful examination, the coherency cube was found to illuminate subtle, often difficult-to-interpret sedimentological and diagenetic features, including dewatering, mass wasting, and karsting events in 3-D seismic data (Haskell et al., 1995).

Although computationally efficient, the original 3-trace  $c_1$  algorithm was somewhat limited in dealing with noisy data. More robust estimates of coherency across 2-D arrays have long been established in seismic velocity analysis (Taner and Koehler, 1969; Key and Smithson, 1990). We therefore quickly

generalized the concept of 2-trace crosscorrelations in the inline and cross-line direction to one of a fully 3-D multitrace cross correlations over a  $J$ -trace analysis window (Figure 1) through the mathematical construct of a  $J$  by  $J$  covariance matrix,  $\underline{\mathbf{C}}$ . The  $(i, j)$ th component of the covariance matrix,  $C_{ij}$ , is simply the crosscorrelation of the  $i$ th trace with the  $j$ th trace in the analysis window. We thus came up with two additional estimates of coherency: our second (or  $c_2$ ) algorithm (Marfurt et al., 1998) was generated by calculating the semblance along various test dip/azimuth pairs from the covariance matrix, whereas our third (or  $c_3$ ) algorithm (Gersztenkorn and Marfurt, 1996a, b), was generated by calculating the eigenvalues of the covariance matrix. These three algorithms and their relationship to the covariance matrix  $\underline{\mathbf{C}}$  are described in the Appendix.

The eigenstructure ( $c_3$ ) algorithm is theoretically superior to the  $c_2$  and  $c_1$  algorithms because it is what mathematicians call

Presented at the 67th Annual International Meeting, Society of Exploration Geophysicists. Manuscript received by the Editor November 19, 1997; revised manuscript received June 12, 1998.

\*AMOCO Expl. & Prod. Technology Group, 4502 East 41st Street, P.O. Box 3385, Tulsa, OK 74102-3385. E-mail: kmarfurt@amoco.com; agersztenkor@amoco.com; snissen@amoco.com.

‡Coherence Technology Corp./Pulsonic, 4343 Second Street NW, Calgary, AB T2K0Z2, Canada. E-mail: sudha@coherence.com.

\*\*Formerly AMOCO Expl. & Prod. Technology Group, 4502 East 41st Street, P.O. Box 3385, Tulsa, OK 74102-3385; presently ARCO Expl. & Prod. Technology, 2300 West Plano Parkway, Plano, TX 75075. E-mail: crawford@sct.arco.com.

© 1999 Society of Exploration Geophysicists. All rights reserved.

a subspace calculation, such that when the signal exceeds the level of additive Gaussian noise, noise is eliminated from the coherency calculation. For this reason, we were very pleased and satisfied when we made our first comparisons of our  $c_3$  algorithm against our  $c_2$  algorithm (Gersztenkorn and Marfurt, 1996a, b). In particular, the  $c_3$  algorithm produces fault traces and channel edges that appear to be both thinner (providing higher lateral resolution) and darker (having greater discrimination between incoherent and coherent events) than that produced by our  $c_2$  algorithm (see Figure 2). We were therefore somewhat disappointed when we saw that our new  $c_3$  coherency estimate failed to produce useful results in areas of strong dip, such as that appearing around the flanks of the salt dome shown in Figures 3a and 4, while our supposedly inferior  $c_2$  algorithm provided quite useful results.

While working on the geologic calibration of the  $c_2$ , or semblance-based coherency algorithm, we noticed that coherency can vary significantly along a fault trace, and fault segments which have relatively high coherence often correspond to areas of locally high dip on dip/azimuth images (e.g., Nissen et al., 1995). Like coherency, dip/azimuth images are powerful tools in mapping faults and other discontinuities (Dalley et al., 1989; Mondt, 1990). We illustrate this phenomenon with the arrows shown on our  $c_2$  coherency image in Figure 4a and on our dip/azimuth image shown in Figure 5. We examine a seismic line AA' that intersects "coherent" sections of an otherwise sharp, low-coherency fault (Figure 3b). Within a local window  $\pm 40$  ms about the 1200-ms time slice, this reflector does indeed appear to be more folded than faulted, even though a more global visual evaluation indicates that this fault continues both above and below the 1200-ms level. In essence, the  $c_2$  algorithm calculation provides us with a correct, though perhaps undesirable, answer. In contrast, we note that the same low-coherency fault trace generated by the  $c_3$

algorithm in Figure 4b is significantly more continuous, showing consistently lower coherency even over this apparently folded area than the same feature generated by our  $c_2$  algorithm in Figure 4a.

Given our inability to map coherency in areas of high structural dip using our high resolution  $c_3$  algorithm, where the lower resolution  $c_2$  algorithm produces useful results, we began our investigation of the effect of dip on all of our coherency algorithms. We will show that an algorithm that calculates coherency along a smoothed estimate of regional dip provides superior results.

### EFFECT OF DIP ON COHERENCY

To illustrate the resolution of our coherency algorithms and their sensitivity to dip, we generated the three simple 2-D synthetic seismograms shown in Figure 6. Our first, noise-free synthetic seismogram (Figure 6a) consists of a flat reflector broken by a fault, thereby producing a 10-ms vertical throw between traces 24 and 25. Our trace spacing is 12.5 m, and our seismic wavelet has a spectrum defined by four corner frequencies of 5, 10, 30, and 70 Hz. In 2-D, our  $c_1$ , or cross-correlation, algorithm reduces to a 2-trace algorithm. Not surprisingly, the fault is invisible to the  $c_1$  algorithm (Figure 7a) since the 10-ms lag crosscorrelation coefficient (see the Appendix) is identically 1.0. What is surprising is the great deal of success we have had using the  $c_1$  algorithm in mapping faults of this size all along. If we had started our work by testing our ideas on such unrealistic synthetic data instead of real data, we would never have stumbled on coherency in the first place! Serendipitously, it is rare that the seismic reflectivity is identical on either side of a fault. In addition to the effects of reflections from the fault

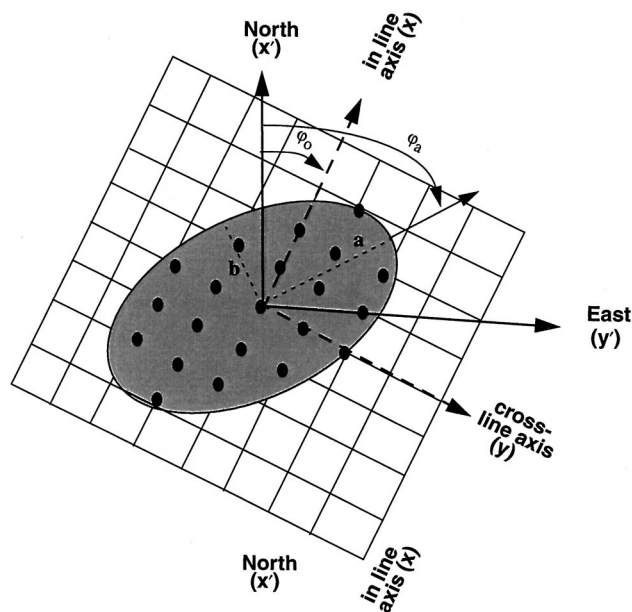


FIG. 1. An elliptical analysis window centered about an analysis point and defined by length of major axis,  $a$ , length of minor axis,  $b$ , and azimuth of major axis,  $\phi_a$ .

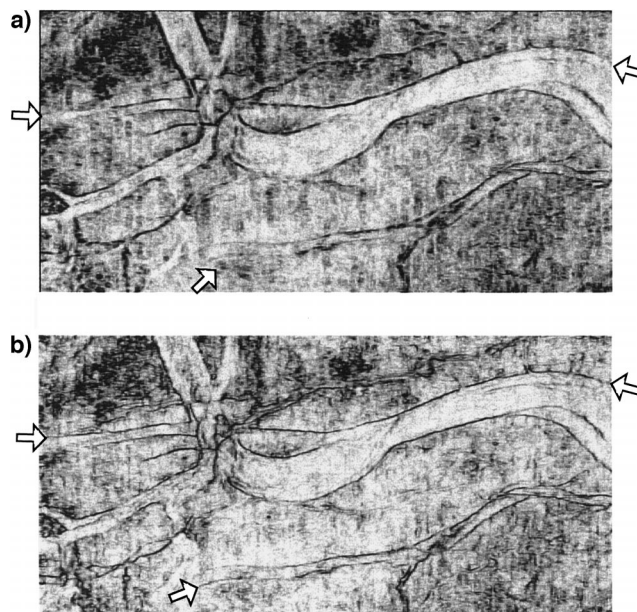


FIG. 2. Seismic coherency estimated using the (a)  $c_2$  algorithm and (b)  $c_3$  algorithm along a smoothed, interpreted seismic horizon containing distributary channels, using a 9-trace, 8-ms analysis window. Note that the channel boundaries appear sharper, indicating higher lateral resolution, and are more continuous in (b), as shown by the arrows.

plane reflector, factors of syntectonic deposition, differential compaction, differential diagenesis, and pressure compartmentalization all work to modify the reflectivity once the faulting has taken place.

In contrast, we note that both the 2-D, 3-trace  $c_2$  semblance-based, and  $c_3$  eigenvalue-based coherency algorithms are sensitive to this subtle fault, with the  $c_3$  estimate being significantly more sensitive to the fault than the  $c_2$  estimate even though there is no noise present. This observation of higher discrimination corroborates our visual evaluation of Figure 2. The lateral resolution of the fault in Figure 7a for both the  $c_2$  and  $c_3$  algorithms appears to be two traces wide.

To evaluate our coherency algorithms in the presence of dip, we construct the synthetic seismogram shown in Figure 6b, which consists of a 2-D dipping reflector having an apparent dip of  $p = 0.25$  ms/m, corresponding to the steep dips seen in Figure 3, and broken by a fault with the same vertical offset of 10 ms as Figure 6a. Once again, our  $c_1$  crosscorrelation algorithm is insensitive to the vertical displacement across the fault and, instead, produces a coherency value of  $c_1 = 1.0$  across the entire profile. Our  $c_2$  algorithm also produces a consistently high value of coherency,  $c_2 = 1.0$ , across the section, but dips to a value of  $c_2 = 0.8$  about the fault. In contrast, although the  $c_3$  algorithm also sees the fault, its background level where there is no faulting hovers about  $c_3 = 0.7$ . This low estimate of

$c_3$  coherency in areas of steep dip correlates to the black zone seen about the steeply dipping salt flanks in Figure 4b.

In an effort to compensate for reflector dip, we generalized our  $c_3$  algorithm to have the same dip sensitivity as our  $c_2$  algorithm. In essence, we explicitly flatten the data over a predetermined number of dips and calculate the  $c_3$  coherency for each dip. Given an interpreter-supplied estimate of the maximum true dip, the actual number of apparent dip pairs,  $(p, q)$ , can be calculated using the Nyquist sampling criterion (e.g., Marfurt et al., 1998). We call this modified or multidip estimate of our  $c_3$  eigenvalue coherency algorithm our  $c_{3,5}$  algorithm and define it as

$$\hat{c}_{3,5} = \max_{p,q} c_3(p, q). \quad (1)$$

If we have  $N_{pq}$  pairs of apparent dip, it is clear that this new  $c_{3,5}$  algorithm will be  $N_{pq}$  times more computationally

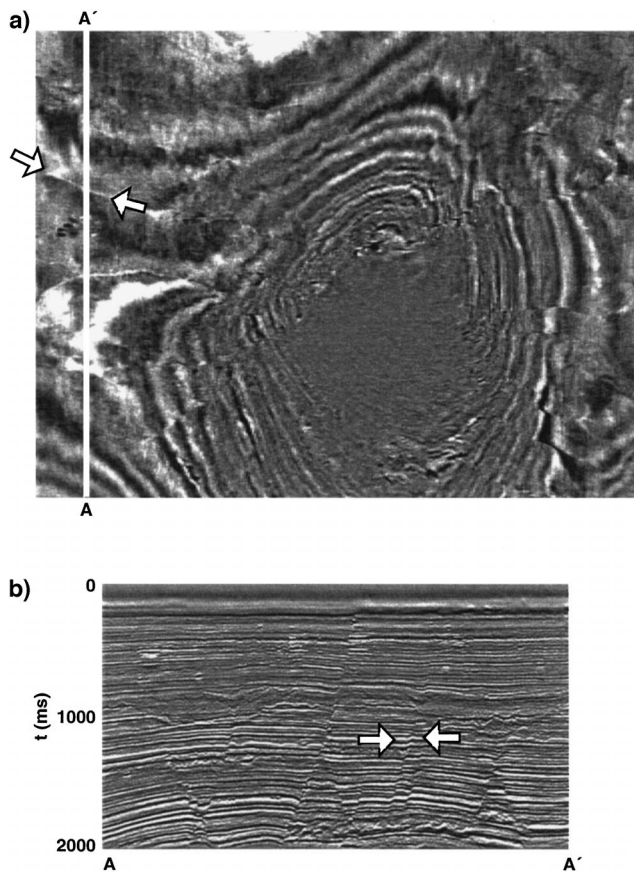


FIG. 3. Seismic data about a salt dome from offshore Louisiana. (a) Time slice at 1200 ms, and (b) vertical seismic section corresponding to line AA'. Arrows in (a) indicate a fault that appears to be a fold in (b). Data courtesy of Geco-Prakla.

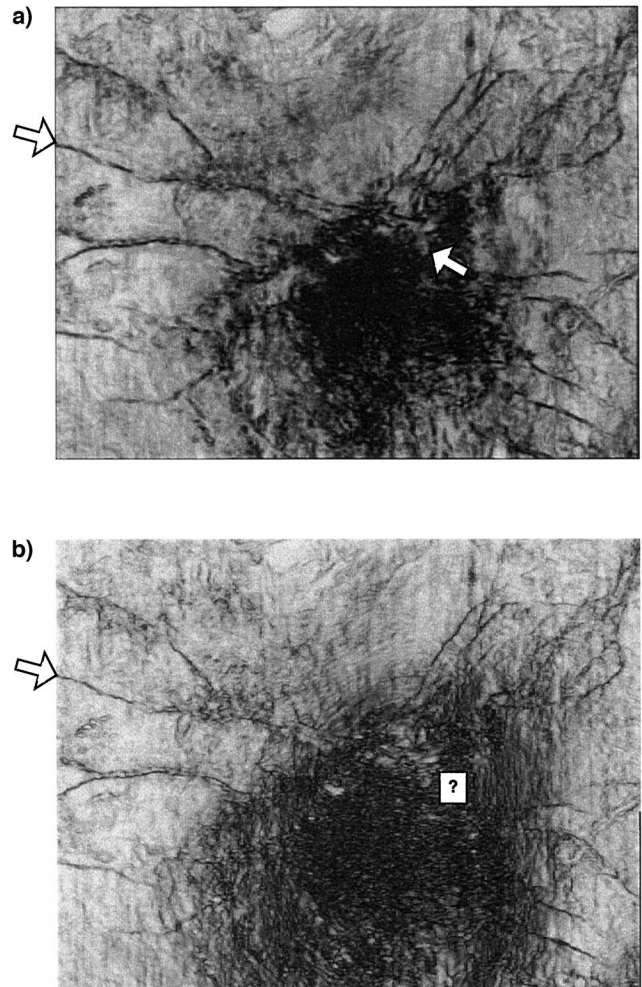


FIG. 4. Horizontal slices at 1200 ms through coherency cubes generated by (a) the multiple dip search  $c_2$  algorithm and (b) the flat dip search  $c_3$  algorithm. The lateral resolution of the  $c_3$  coherency algorithm is superior except near the steep dip flanks of the salt dome. Near the salt, the  $c_2$  coherency image shows the “radial” fault demarcating coherent reflectors to the north from the incoherent salt to the south. The arrows correspond to the fault indicated by arrows in Figure 3.

expensive than our  $c_3$  algorithm. Unfortunately, whereas this  $c_{3,5}$  estimate of coherency correctly compensates for dip in areas where there is no faulting (as shown in Figure 7b), it provides no greater fault resolution than the significantly more economic semblance algorithm. Worse yet, the high fault discrimination in  $c_3$  coherency seen for the flat dip reflector in Figure 7a has reverted to that of the lower discrimination  $c_2$  coherency for this new, more expensive  $c_{3,5}$  algorithm. Examination of the apparent dip pair associated with equation (1) shows that the maximum coherency occurs for an apparent dip that is not indicative of the reflector geometry, but rather of the local fault-induced reflector offset. Clearly, if we can better estimate a less local, or smoother, estimate of apparent dip, we will be able to more accurately estimate abrupt local changes in reflector offset using the coherency attribute.

We therefore discard our inefficient, low-resolution  $c_{3,5}$  algorithm and develop a new  $c_{3,6}$  algorithm that calculates an eigenvalue estimate of coherency along a smoothed, more regional dip. To achieve this end, we first estimate  $(p, q)$  at each point of our seismic cube using the computationally efficient  $c_2$  or semblance-based algorithm. We next smooth this estimate of  $(p, q)$  by either calculating its mean, median, or alpha-trimmed mean over a window approximately 10 times larger

than our original coherency analysis window to obtain  $(\bar{p}, \bar{q})$ . The seismic data in the analysis window are next flattened using this smoothed dip,  $(\bar{p}, \bar{q})$ , after which we calculate the  $c_{3,6}$  coherency:

$$\hat{c}_{3,6} \equiv c_3(\bar{p}, \bar{q}). \quad (2)$$

An alternative, somewhat more expensive, method would be to perform our dip/azimuth analysis using a large window. The data are then flattened and the  $c_{3,6}$  coherency calculated in a small analysis window.

We note that this new, hybrid semblance-eigenvalue,  $c_{3,6}$  algorithm estimate of coherency in Figure 7b correctly estimates a value of  $c_{3,6} = 1.0$  in areas of continuous reflector dip, yet shows a greater relative deflection at the fault than either our  $c_2$  or  $c_3$  algorithms. In Figures 6c and 7c, we evaluate these algorithms for a signal to noise ratio of 1:1. Although the  $c_1$  algorithm is insensitive to the vertical offset across a fault of an otherwise coherent reflector, it is quite sensitive to changes in incoherent noise, such that the results are totally erratic. In contrast to Figures 7a and 7b, the  $c_2$  and  $c_{3,5}$  estimates of coherency now differ because of the exclusion of the “noise” components of the data in the eigenvalue calculation as

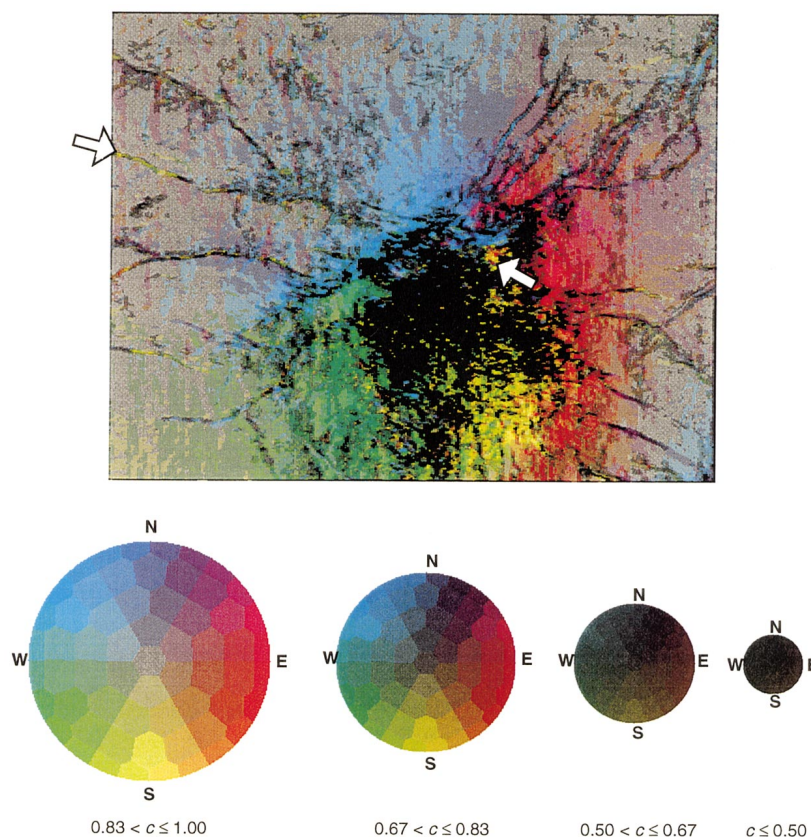


FIG. 5. Dip/azimuth calculated using our  $c_2$  or semblance algorithm. Color legend corresponds to the discrete dip/azimuth pairs searched, with zero dip,  $d = 0.0$  ms/m, being indicated by gray at the center of the legend, and pure colors corresponding to a dip  $d = 0.25$  ms/m along the perimeter of the legend. Pastel colors correspond to high-coherency reflectors,  $0.83 < c \leq 1.00$ . Black corresponds to low-coherency reflectors,  $c \leq 0.50$ . Note that the radial fault delineated by arrows appears intermittently as yellow, indicating a coherent event having locally steep dip to the south, such as seen in Figure 3b.

described in Gersztenkorn and Marfurt (1996a, b), although the algorithm gets confused as to what is signal and what is noise in a 3-trace algorithm with such high noise. The 2-D, 3-trace  $c_{3,6}$  algorithm indicates the presence of the fault better than the other algorithms, although there are several other local, noise-induced false drops in coherency. These coherency artifacts will be randomly distributed with respect to a continuous fault trace or channel edge on a time slice through a 3-D coherency cube, and are therefore not overly troublesome. Nevertheless, we also expect to obtain more robust, though lower resolution, results by incorporating five traces into our 2-D  $c_{3,5}$  coherency calculation.

In Figure 7d, we compare coherency estimated by our 3-trace  $c_1$  algorithm to our 5-trace  $c_2$ ,  $c_3$ ,  $c_{3,5}$  and our newest  $c_{3,6}$  algorithms for the noise contaminated data shown in Figure 6c. The 3-trace  $c_1$  estimate of coherency is simply repeated for reference from Figure 7c. The  $c_2$  coherency estimate of the fault is improved by including the additional two traces. The  $c_3$  algorithm estimate degrades, because it can consider only the flat component of the dipping reflector as signal, with everything else being considered as different parts of the noise spectrum. The new  $c_{3,6}$  algorithm behaves very nicely, unambiguously delineating the fault, though of course with less lateral resolution than with the 3-trace algorithm shown in Figure 7c.

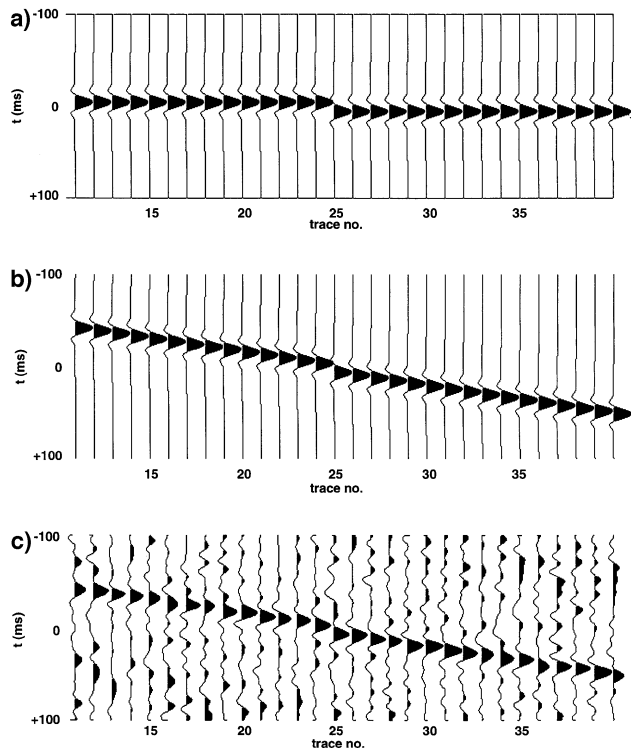


FIG. 6. Synthetic seismograms used in calibrating sensitivity of various coherency algorithms to reflector dip and to the presence of noise. Trace spacing,  $\Delta x = 12.5$  m. Wavelet generated with corner frequencies of 5, 10, 30, and 70 Hz. Fault offset is 10 ms. (a) Noise-free synthetic seismogram with flat dip,  $p = 0.0$  ms/m. (b) Noise-free synthetic seismogram with dip  $p = 0.25$  ms/m. (c) Synthetic seismogram with signal to noise ratio = 1:1 and dip  $p = 0.25$  ms/m.

## APPLICATION AND DISCUSSION

We now return to our salt dome example shown in Figures 3 and 4. Since the azimuth has a discrete jump between values of  $-180$  and  $+180$  degrees, there is no simple way to smooth the

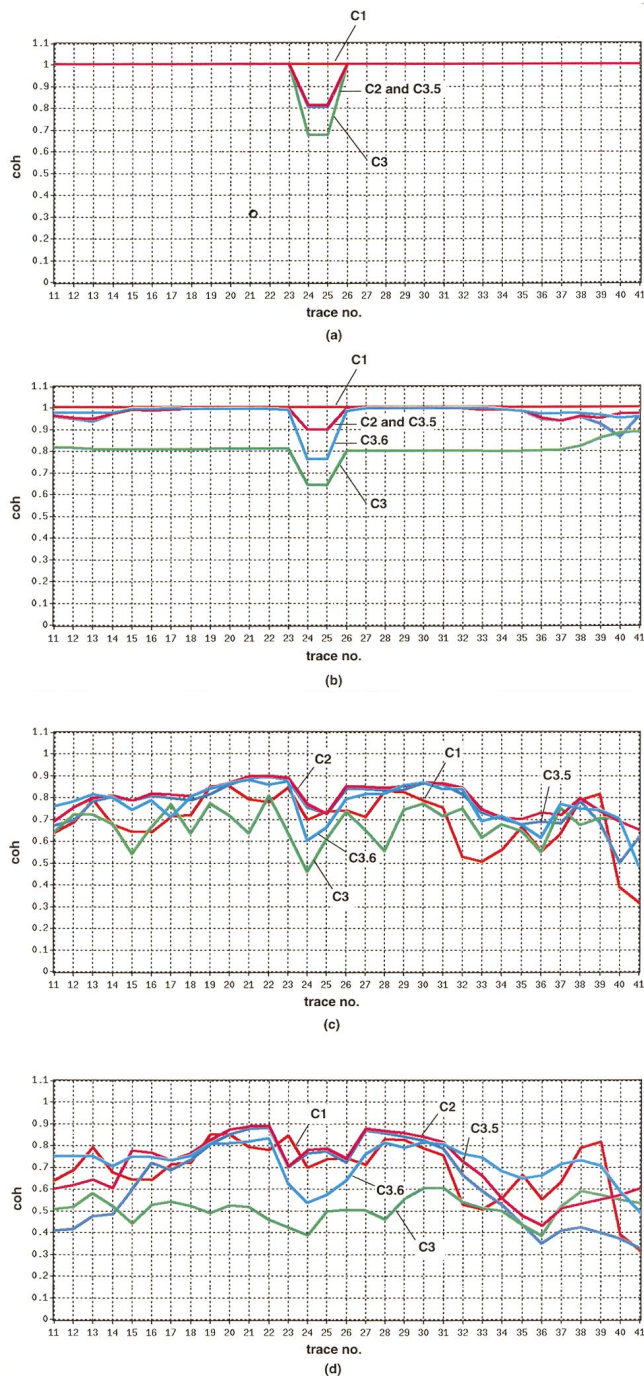


FIG. 7. Coherency calculated using different coherency algorithms. (a), (b), and (c) correspond to Figures 6a–c using 2-D, 2-trace  $c_1$  algorithm, and 3-trace  $c_2$ ,  $c_3$ ,  $c_{3,5}$ , and  $c_{3,6}$  algorithms. Note that the  $c_1$  algorithm is insensitive to the noise-free faults. Dip smoothing included  $\pm 10$  traces for the  $c_{3,6}$  algorithm. (d) Coherency calculated using 5-trace 2-D  $c_2$ ,  $c_3$ ,  $c_{3,5}$ , and  $c_{3,6}$  algorithms for the data shown in Figure 6c. Vertical analysis window is  $\pm 50$  ms for all algorithms.

dip/azimuth ( $d, \phi$ ) data cube shown in Figure 5. We therefore convert it to the two apparent dip components, ( $p, q$ ), using:

$$p = d \cos \phi, \quad \text{and} \quad q = d \sin \phi, \quad (3)$$

where the azimuth,  $\phi$ , is measured clockwise from the north. The results are displayed in Figure 8. We are now free to smooth these apparent dips over a  $500 \times 500$  m ( $21 \times 11$  trace) window, resulting in the blurred images shown in Figure 9. We calculate our eigenvalue-based coherency along these smoothed apparent dips, ( $\bar{p}, \bar{q}$ ), thereby generating our  $c_{3,6}$  estimate of coherency shown in Figure 10. We note that the resolution in the area of flat dip is equivalent to that of Figure 4b. However, we are now able to carry these higher resolution results into the areas of strong structural dip about the flanks of the salt dome. The fault trace indicated by arrows is both more continuous and can be carried further than the fault trace on either Figure 4a or 4b.

Reexamining Figure 2 with this improved understanding of how our coherency algorithms respond to structural dip, we

recall that this coherency image was generated along a structurally deformed, interpreter picked horizon. After significant smoothing of the picks, the seismic data were subsequently palinspastically restored, or flattened, before calculating the coherency. The  $c_2$  estimate of coherency in Figure 2a was generated using a 61-angle search for maximum coherency. The  $c_3$  estimate of coherency in Figure 2b was calculated using a single-angle search for coherency, that is, the covariance matrix was formed after flattening the seismic traces along the interpreted horizon, without the application of any additional time shifts. Although the  $c_2$  algorithm theoretically has lower resolution than the eigenvalue method for noisy data, it also suffers in that it searches for maximum coherency along additional candidate dips centered about the now flattened horizon. This generates an image that looks somewhat more coherent, much like the fault indicated by arrows in Figure 3a. We now realize that our  $c_3$  algorithm applied to this flattened horizon is equivalent to what we would ideally obtain by our new  $c_{3,6}$  algorithm if the coherency were first calculated and then extracted from the structurally deformed horizon. Instead of estimating

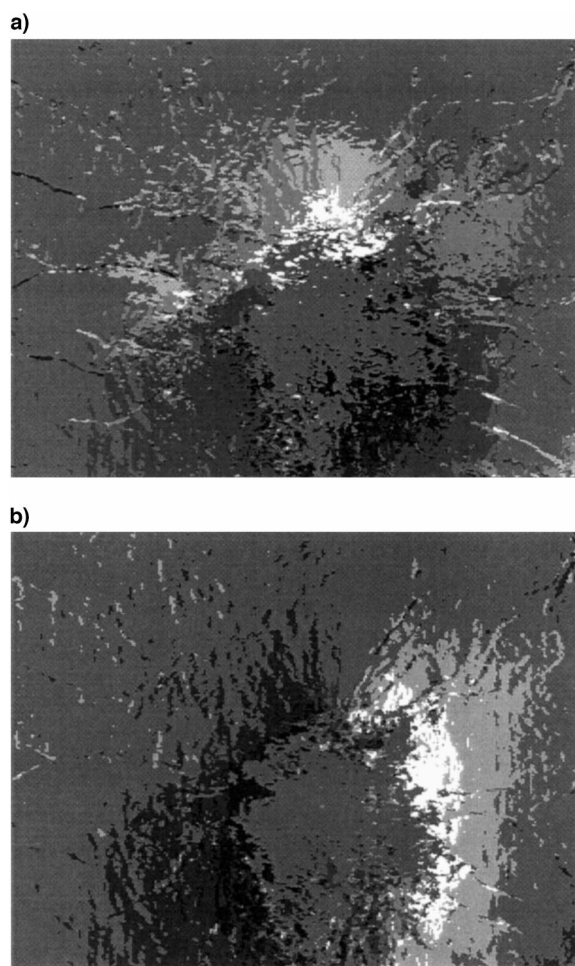


FIG. 8. Apparent (a) in-line dip,  $p$ , and (b) cross-line dip,  $q$ , generated from the discrete dip search  $c_2$  semblance-based coherency algorithm. Trace spacings are  $\Delta x = 25$  m, and  $\Delta y = 50$  m. White indicates positive (downward) dip in the (a)  $x$  (north) and (b)  $y$  (east) directions.

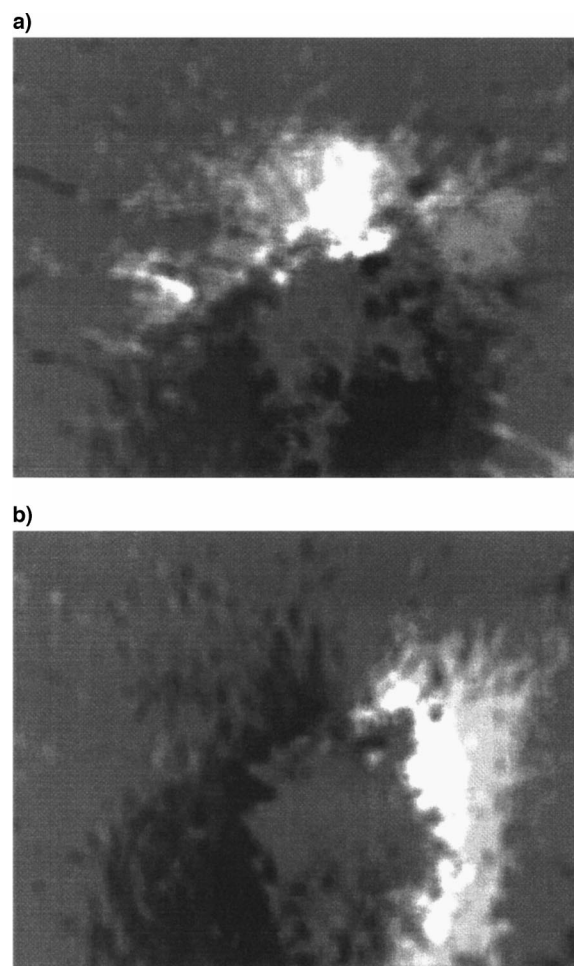


FIG. 9. Smoothed version of (a)  $p$  and (b)  $q$  shown in Figure 8 obtained by independently averaging each apparent dip over a  $\pm 250$ -m window.

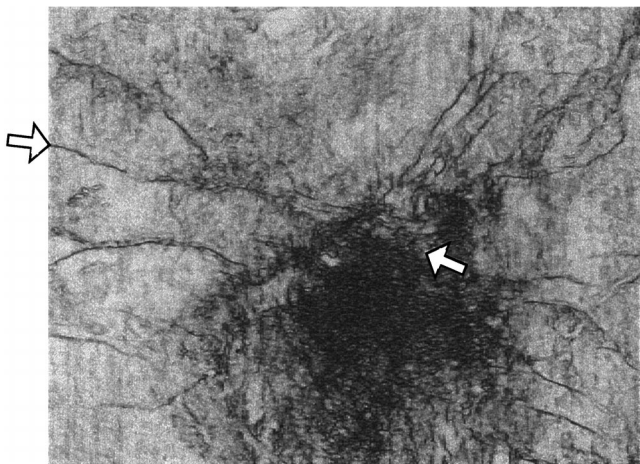


FIG. 10. Horizontal slice at 1200 ms through the coherence cube generated using the eigenstructure algorithm operating along the smoothed dips shown in Figure 9. Note that the lateral resolution is equivalent to that of Figure 4b in areas of shallow dip, yet provides quality images of improved resolution over Figure 4a in areas of steep dip. The arrows correspond to the fault indicated by arrows in Figure 3.

non-local reflector dip by use of our semblance algorithm and subsequent smoothing, we have estimated this dip via the process of an interpreter picking the horizon. In principle, such interpreter-guided picking is the optimal means of estimating reflector dip, thereby substantiating the results seen in Figure 2.

### CONCLUSIONS

We have shown both how our various coherence algorithms are sensitive to structural dip and how, through a hybrid technique, we have developed an algorithm that produces superior coherence estimates in areas of both low and high dip. We are not surprised but somewhat sobered that if there is no change of the seismic wavelet across a fault, our original crosscorrelation algorithm would not have seen it. Fortunately, changes in reflectivity caused by differential diagenesis, pressure compartmentalization, and syntectonic deposition that are often associated with faulting, as well as the interference of fault plane reflections and mismigration due to seismic velocity changes, all give rise to measurable coherence variations across a fault that are detectable by our original algorithm. Our second-generation multitrace semblance-based coherence algorithm is sensitive to the vertical displacement of otherwise identical reflectors across a fault. However, what we numerically estimate is not the coherence across the fault, but rather the coherence of a postulated reflector segment that best fits the (vertically offset) data within the numerical analysis window. By definition, this coherence estimate will always be greater than or equal to an estimate of coherence projected along a dip parallel to the reflector across the fault. This leads to a local wash out of what we would otherwise like to interpret as low-coherence discontinuities, producing images that have both reduced lateral resolution and reduced contrast. Our third-generation multitrace eigenstructure analysis-based coherence algorithm

provides optimum lateral resolution in the presence of noise. For reasons of computational efficiency, this original algorithm did not explicitly search over a suite of trial dips for maximum coherence. Generalizing this algorithm to do this explicit search allowed us to map coherence in the presence of steep dip, but unfortunately, at least in areas of flat dip having a high signal-to-noise ratio, reduced our lateral resolution and contrast to that of our semblance algorithm.

We address the problem of local apparent dip by constructing a hybrid algorithm. We begin by estimating the apparent dips everywhere in the cube using our most efficient, though lower resolution, semblance algorithm. These dips are then smoothed over a large window using either median, alpha-trimmed mean, or mean filters to provide a robust estimate of reflector versus local seismic dip. We then calculate our eigenstructure estimate of coherence only along the dip of the reflector, thereby providing maximum lateral resolution of reflector discontinuities.

We are also now able to understand some of our exciting early coherence results calculated along picked horizons having considerable structural deformation. In this situation, we simply flatten the seismic data along this horizon and calculate our eigenstructure estimate of coherence using our original, flat dip algorithm. In essence, this method is identical to our hybrid method, except that in the flattening case, our estimate of reflector dip has been implicitly estimated by the interpreter who picks the seismic reflector horizon.

### ACKNOWLEDGMENTS

We are grateful to Julie Youngblood and Vicki Wilson of Amoco's Tulsa Technology Center Document Services for their care in putting this document together.

### REFERENCES

- Bahorich, M. S., and Farmer, S. L., 1995, 3-D seismic coherence for faults and stratigraphic features: *The Leading Edge*, 1053–1058.
- , 1996, Methods of seismic signal processing and exploration: U.S. Patent 5 563 949.
- Dalley, R. M., Gevers, E. E. A., Stampli, G. M., Davies, D. J., Gastaldi, C. N., Ruijtenberg, P. R., and Vermeer, G. J. D., 1989, Dip and azimuth displays for 3-D seismic interpretation: *First Break*, 7, 86–95.
- Gersztenkorn, A., and Marfurt, K. J., 1996a, Coherence computations with eigenstructure: 58th Internat. Mtg., Eur. Assn. Geoscientist and Engineers, Extended Abstracts, x031.
- , 1996b, Eigenstructure based coherence computations: 66th Ann. Internat. Mtg., Soc. Expl. Geophys., Expanded Abstracts, 328–331.
- Haskell, N. L., Nissen, S. E., Lopez, J. A., and Bahorich, M. S., 1995, 3-D seismic coherence and the imaging of sedimentological features, *in* Predictive high resolution sequence stratigraphy: Norwegian Petrol. Soc. Conf.
- Key, S. C., and Smithson, S. B., 1990, New approach to seismic reflection event detection and velocity determination: *Geophysics*, 55, 1057–1069.
- Marfurt, K. J., Kirlin, R. L., Farmer, S. L., and Bahorich, M. S., 1998, 3-D seismic attributes using a running window semblance algorithm: *Geophysics*, 63, 1150–1165.
- Mondt, J. C., 1990, The use of dip and azimuth horizon attributes in 3-D seismic interpretation: SPE Paper 20943, 71–77.
- Nissen, S. E., Haskell, N. L., Lopez, J. A., Donlon, T. J., and Bahorich, M. S., 1995, 3-D seismic coherence techniques applied to the identification and delineation of slump features: 65th Ann. Internat. Mtg., Soc. Expl. Geophys., Expanded Abstracts, 1532–1534.
- Taner, M. T., and Koehler, F., 1969, Velocity spectra-digital computer derivation and applications of velocity functions: *Geophysics*, 41, 441–463.

## APPENDIX

## RELATIONSHIP OF COHERENCY TO THE COVARIANCE MATRIX

Given  $J$  seismic traces containing data,  $u_j$ , having coordinates  $(x_j, y_j)$  within our analysis window shown in Figure 1, we calculate the  $2M + 1$  sample covariance matrix,  $\mathbf{C}$ , along a pair of apparent dips,  $(p, q)$ , centered about time,  $t = n\Delta t$ , to be:

$$\mathbf{C}(p, q) = \sum_{m=n-M}^{n+M} \begin{pmatrix} \bar{u}_{1m}\bar{u}_{1m} & \bar{u}_{1m}\bar{u}_{2m} & \dots & \bar{u}_{1m}\bar{u}_{Jm} \\ \bar{u}_{2m}\bar{u}_{1m} & \bar{u}_{2m}\bar{u}_{2m} & \dots & \bar{u}_{2m}\bar{u}_{Jm} \\ \vdots & \vdots & \ddots & \vdots \\ \bar{u}_{Jm}\bar{u}_{1m} & \bar{u}_{Jm}\bar{u}_{2m} & \dots & \bar{u}_{Jm}\bar{u}_{Jm} \end{pmatrix}, \quad (\text{A-1})$$

where  $\bar{u}_{jm} = u_j(m\Delta t - px_j - qy_j)$  indicates the seismic traces interpolated along the apparent dip at time,  $t = m\Delta t - px_j - qy_j$ .

**The  $c_1$  algorithm**

For the 2-D, 2-trace  $c_1$  algorithm, the coherency along  $(p, q = 0)$  is

$$c_1(p, q = 0) = \frac{C_{12}}{(C_{11}C_{22})^{1/2}}. \quad (\text{A-2})$$

For the 3-D, 3-trace  $c_1$  algorithm, the coherency along  $(p, q)$  is

$$c_1(p, q) = \left[ \frac{C_{12}}{(C_{11}C_{22})^{1/2}} \frac{C_{13}}{(C_{11}C_{33})^{1/2}} \right]^{1/2}. \quad (\text{A-3})$$

Our coherency estimate,  $\hat{c}_1$ , is then the maximum coherency found along the dips searched:

$$\hat{c}_1 = \max_{p,q} c_1(p, q). \quad (\text{A-4})$$

**The  $c_2$  algorithm**

We calculate our  $c_2$  estimate of coherency along an apparent dip,  $(p, q)$ , by

$$c_2(p, q) = \frac{\mathbf{a}^T \mathbf{C} \mathbf{a}}{J \text{Tr}(\mathbf{C})}, \quad (\text{A-5})$$

where  $\mathbf{a}$  is a  $J$  element vector given by:

$$\mathbf{a} = \begin{bmatrix} 1 \\ 1 \\ \vdots \\ 1 \end{bmatrix}, \quad (\text{A-6})$$

and  $\text{Tr}(\mathbf{C})$  denotes the numerical trace of the covariance matrix

$$\text{Tr}(\mathbf{C}) = \sum_{j=1}^J C_{jj}. \quad (\text{A-7})$$

Again, our estimate of coherency,  $\hat{c}_2$ , is the maximum coherency found along the dips searched:

$$\hat{c}_2 = \max_{p,q} c_2(p, q). \quad (\text{A-8})$$

**The  $c_3$  algorithm**

We calculate our  $c_3$  estimate of coherency along a dip,  $(p, q)$ , by

$$c_3(p, q) = \frac{\lambda_1}{\sum_{j=1}^J \lambda_j}, \quad (\text{A-9})$$

where  $\lambda_j$  is the  $j$ th eigenvalue of the covariance matrix,  $\mathbf{C}$ . Our original  $c_3$  (eigenstructure coherence) algorithm as described by Gersztenkorn and Marfurt (1996a, b), produced a coherency estimate

$$\hat{c}_3 = c_3(p = 0, q = 0). \quad (\text{A-10})$$

This algorithm is readily generalized to one that searches over multiple dips, which we denote as a  $\hat{c}_{3.5}$  estimate of coherency in Figure 7:

$$\hat{c}_{3.5} = \max_{p,q} c_3(p, q). \quad (\text{A-11})$$